



1 Impact of lower atmospheric scattering on ground-based optical 2 thermospheric wind observations with spatially uneven airglow

3 Xiaolong Wei^{1,2,4}, Guoying Jiang^{1,3,4,*}, Yajun Zhu^{1,3,4,*}, Jiyao Xu^{1,4}, Weijun Liu^{1,4}, Tiancai Wang^{1,2,4},
4 Guangyi Zhu^{1,4}, Wei Yuan^{1,4}

5 ¹State Key Laboratory of Solar Activity and Space Weather, National Space Science Center, Chinese Academy of Sciences,
6 Beijing, 100190, China

7 ²College of Earth and Planetary Sciences, University of Chinese Academy of Sciences, Beijing, 100049, China.

8 ³School of Astronomy and Space Science, University of Chinese Academy of Sciences, Beijing, 100049, China.

9 ⁴Hainan National Field Science Observation and Research Observatory for Space Weather, Hainan, 571734, China

10 *Correspondence to: Guoying Jiang (gyjiang@spaceweather.ac.cn), Yajun Zhu (y.zhu@swl.ac.cn)

11 **Abstract.** Scattered airglow emissions in the lower atmosphere can bias ground-based interferometer observations of
12 thermospheric winds, particularly when airglow brightness becomes spatially uneven due to auroras. During two geomagnetic
13 storms with visible auroras on May 10th and Oct. 10th, 2024, the Doppler Asymmetric Spatial Heterodyne (DASH) and Fabry-
14 Perot (FP) interferometers concurrently detected atypical winds at Siziwang (SIZW, 41.83° N, 111.93° E), suspected to be
15 caused by scattering. These atypical winds, characterized by horizontal differences exceeding 400 m·s⁻¹ between opposite
16 cardinal directions (N-S or E-W) and downwelling exceeding 100 m·s⁻¹, showed a strong temporal association with airglow
17 brightness. By modelling the transmission of scattered airglow emissions, we calculated post-scattering wind speeds as the
18 initial wind speeds weighted by both scattered and direct intensities. With fixed initial speeds, the simulation reproduced the
19 temporal characteristics of the atypical winds, demonstrating that scattering causes these intense horizontal differences and
20 downwelling. The simulation also shows that the scattering-induced biases have directional inhomogeneity with characteristics
21 linked to the location and background line-of-sight speed of the brighter airglow region. The commonly used horizontal
22 average wind may experience numerical deviations due to directional inhomogeneity. The accuracy of the simulation is limited
23 by the accuracy of airglow observations and atmospheric optical depth.

24 1 Introduction

25 Optical interferometers are widely utilized to observe thermospheric neutral wind (Burnside et al., 1981; Burnside and Tepley,
26 1989; Killeen et al., 1995; Emmert et al., 2001; Fejer et al., 2002; Emmert et al., 2006; Wu et al., 2014). Thermospheric wind
27 can be derived from measuring the Doppler shift of OI red-line airglow emission at 630.0 nm. This emission, primarily from
28 the collisional deactivation of O(¹D) generated by O₂⁺ dissociative recombination, peaks near 250 km altitude. The height-
29 integrated thermospheric wind around the peak altitude can be obtained (Biondi and Feibelman, 1968; Hernandez and Roble,
30 1976; Burnside et al., 1981; Biondi et al., 1995; Nakajima et al., 1995). For scanning interferometers, three-dimensional wind
31 vectors can be derived by observing the zenith and four cardinal directions at a specific elevation angle. The scanning range



covers a circular area about 500 km in diameter at airglow altitude. Given thermospheric wind uniformity at this scale, horizontal winds observed in two opposite cardinal directions (N-S or E-W) are typically similar. Averaging opposite cardinal directions improves accuracy, mitigates cloud effects, and is typically used to represent local meridional or zonal winds even during geomagnetic storms (Friedman and Herrero, 1982; Fejer et al., 2002; Sakanoi et al., 2002; Dhadly et al., 2017; Huang et al., 2018; Xu et al., 2019; Li et al., 2023; Wang et al., 2025).

However, horizontal winds in opposite cardinal directions occasionally show significant separation exceeding 100 m s^{-1} , with strong vertical winds generally deviating from typical thermospheric wind uniformity. These observations often occur near auroras, unaffected by clouds or moonlight, and have acceptable standard errors. They mainly occur in polar regions (Crickmore et al., 1991; Price et al., 1995; Smith and Hernandez, 1995; Innis et al., 1999; Ishii et al., 2001; Guo and McEwen, 2003; Anderson et al., 2012), but have also been seen at mid-latitudes during major magnetic storms (Hernandez and Roble, 1976; Makela et al., 2014).

Atmospheric scattering of airglow emissions introduces errors to ground-based interferometers, potentially accounting for these atypical wind observations. Initially, it was thought to impact airglow peak height measurements by photometers (Ashburn, 1954). Subsequent studies by Abreu et al. (1983) explored its impact on thermospheric wind speed measurements using a Fabry-Perot interferometer. Harding et al. (2017a; 2017b) later systematically modelled and estimated these effects, revealing that scattering was responsible for the anomalous vertical winds observed at mid-latitudes during geomagnetic storms by Makela et al. (2014). Light from brighter airglow regions scatters omnidirectionally in the lower atmosphere, primarily the troposphere and stratosphere, and is detectable outside its original direction. The additional Doppler shift of this scattered light can bias the retrieval of line-of-sight (LOS) speeds as well as the converted horizontal and vertical winds. Scattering-induced biases are more pronounced during spatially uneven airglow brightness, such as during auroras (Harding et al., 2017a). Uneven airglow brightness refers specifically to inhomogeneous red-line emissions. Airglow and auroral emissions have similar wavelengths and peak heights, though differing in mechanism, making them hard to distinguish in ground-based observations. Harding et al. (2017b) also investigated the impact of atmospheric scattering on interferometer wind and temperature measurements during quiet periods and attempted to correct for the associated errors. Additionally, spectral contamination from precipitating energetic ions can also bias interferometers (Makela et al., 2014). They suggested that the enhanced downwelling at mid-latitudes during storms might result from the contamination of the spectral profile by fast O atoms associated with the influx of low-energy O^+ ions.

From a dynamical perspective, wind differences in opposite cardinal directions are considered horizontal divergence, which are often associated with changes in vertical winds. Near the aurora arc, these atypical winds are mainly caused by ion drag, Joule heating, and energy particle precipitation (Hays et al., 1984; Rees et al., 1984; Conde and Smith, 1995; Conde et al., 2001; Anderson et al., 2012). Generally, excessive horizontal divergence and vertical wind appear alongside rapidly changing auroras and exhibit a matching spatial relationship that upward (downward) winds accompanied by divergences (convergences)



64 are often detected when aurora exists equatorward (poleward) of the observatory (Ishii et al., 2001; Guo and McEwen, 2003).
65 The combination of vertical wind and horizontal divergence is related to gravity waves excited by the above processes in polar
66 regions, presenting a wave-like structure and phase delay between vertical and horizontal wind components. (Price et al., 1995;
67 Smith and Hernandez, 1995; Ishii et al., 1999; Ishii et al., 2001; Shinagawa and Oyama, 2006). At mid-latitudes, which are
68 not primary regions for magnetospheric energy injection, atypical winds are instead related to the propagation of gravity waves
69 from polar regions. (Hernandez and Roble, 1976).

70 During two geomagnetic storms with visible auroras, we observed similar atypical winds in ground-based interferometers at
71 Siziwang (SIZW, 41.83° N, 111.93° E), China. These winds showed intense differences over 400 m·s⁻¹ in two opposite cardinal
72 directions for both meridional and zonal components, along with downward wind exceeding 100 m·s⁻¹. The observations were
73 unaffected by moonlight or clouds, and the interferometer retrieval errors were acceptable. These atypical winds at SIZW only
74 occurred with auroras and significantly deviated from the regional climatological norms over the China region (Jiang et al.,
75 2018; Yang et al., 2020). This raises the question of whether the atypical winds are driven by dynamical processes or by
76 scattering-induced biases of interferometers, which causes the thermospheric wind to deviate from horizontal uniformity.
77 Unfortunately, both factors can manifest as increased differences between opposite cardinal directions, complicating the
78 distinction between them (Harding et al., 2017a). However, the simultaneous variations in vertical winds, horizontal
79 differences, and red-line brightness show no phase lag, thus not providing evidence for the energy conversion process (Ishii et
80 al., 1999). Instead, these variations resemble a systematic error, as they all involve negative LOS speeds. This suggests that
81 scattering impact may be more significant than dynamic mechanisms in these cases.

82 Auroras are rare at mid-latitudes in East Asia due to low magnetic latitude. The magnetic latitude of SIZW is just 37.7° N. But
83 increased solar activity has led to more frequent sightings of mid-latitude red auroras in Japan and China (Kataoka et al., 2024a;
84 Kataoka et al., 2024b; Ma et al., 2024). Previously overlooked, the scattering-induced biases associated with auroras need
85 further analysis to determine the accuracy and suitability of storm-time observations for dynamical analysis. While prior
86 studies have examined vertical wind biases of Fabry-Perot interferometers under auroral conditions (Abreu et al., 1983;
87 Harding et al., 2017a; Harding et al., 2017b), we will incorporate Doppler Asymmetric Spatial Heterodyne (DASH)
88 interferometer data to compare scattering impact across different interferometer types. Additionally, we will investigate the
89 causes and patterns of horizontal differences and assess the reliability of individual directions and horizontal average winds
90 under the influence of scattering. In the following text, a scattering radiative transfer model is used to simulate interferometer
91 observations in two cases with visible aurora. The presence and patterns of scattering-induced biases are analyzed by
92 comparing simulations with observations.



93 2 Instruments and model

94 This study was conducted at the Siziwang station (SIZW; 41.83° N, 111.93° E, and 37.7° N MLat) of the Chinese Meridian
95 Project Phase II (Wang et al., 2024), utilizing a Dual-Channel All-sky Airglow Imager (DCAI), a Dual-Channel Optical
96 Interferometer (DCOI), and a Fabry-Perot Interferometer (FPI). DCOI derives neutral winds by observing atomic oxygen
97 green-line (557.7 nm, around 96 km) and red-line (630.0 nm, around 250 km). DCAI observes hydroxyl (around 87 km) and
98 atomic oxygen red-line nightglow, respectively. FPI only works at the red-line. Our focus is on the red-line channel. Using
99 DCAI images as one of the inputs, wind biases from optical interferometers can be simulated by a scattering radiative transfer
100 model (scattering model for short). Instruments and the model are described in the following subsections.

101 2.1 Dual-Channel All-Sky Airglow Imager

102 Dual-Channel All-Sky Airglow Imager (DCAI) comprises a fisheye lens with an approximate 170 degree field of view, a 2
103 nm narrow-band filter, and a 1024×1024 pixel, 16 bit cooled CCD. DCAI exposure time of the red-line is 2 minutes. The
104 obtained airglow images are first calibrated to the local spherical coordinate system, then sequentially corrected for stray light,
105 Van Rhijn effect, and atmospheric extinction, and finally projected onto the 250 km airglow plane. Due to DCAI not calibrating
106 the Rayleigh unit (Shiokawa et al., 2000), observed brightness is only normalized to the full-well value. And because of fish-
107 eye lens distortion and the lack of Rayleigh unit calibration, the edge brightness of the view is inaccurate. Thus, observations
108 are restricted within a 70° zenith angle. For larger zenith angles, the brightness is obtained by radial zero-order extrapolation
109 in airglow projection. Detailed image processing procedures are in Appendix B.

110 2.2 Dual-channel optical interferometer

111 Dual-channel optical interferometer (DCOI) is a scanning interferometer using Doppler Asymmetric Spatial Heterodyne
112 (DASH) technology. DASH exhibits a wider field of view, better thermal stability, simplified mechanisms, and lower tolerance
113 requirements than other interferometer structures (Englert et al., 2007; Englert et al., 2010; Harlander et al., 2017; Wei et al.,
114 2020). DCOI consists of a 630 nm narrow-band filter (2 nm bandwidth), a 9 degree field-of-view lens (f/6), a DASH
115 interferometer with a 25 mm aperture, a Neon lamp for calibration, and a 2048×2048 pixel CCD (13.5 μm per pixel) (Wei et
116 al., 2020; Zhu et al., 2023; Liu et al., 2025). Its thermal stability is maintained within 0.1 K. DCOI measures three-dimensional
117 wind speeds by scanning five directions (zenith and four cardinal directions at 45° zenith angle). Each direction is exposed for
118 5 minutes, completing a cycle roughly every 25 minutes. DCOI adopts an observation with the smallest error after evening as
119 the reference zero wind speed. The slant LOS speeds are subtracted by the time-regressed projection of vertical speed and then
120 converted to horizontal using the sine of zenith angles. It is worth noting that during auroral events, vertical winds with absolute
121 values exceeding 50 m·s⁻¹ are excluded from the regression, as they contain scattering effects that could introduce additional
122 biases to other directions. DCOI provides two series of meridional wind, two series of zonal wind, and one series of vertical
123 wind.



124 2.3 Fabry-Perot Interferometer

125 Fabry-Perot Interferometer (FPI), as a mature solution, conducts comparative observations with DCOI. It features a 630 nm
126 narrow-band filter (2 nm bandwidth), a 2.54 degree field-of-view lens ($f/6$), a 50 mm aperture etalon with a 7 mm gap, a
127 frequency-stabilized laser for calibration, and a 1024×1024 pixel CCD (13 μm per pixel). FPI uses the same integration time
128 and scanning method as DCOI to obtain horizontal and vertical winds for each cardinal direction and zenith. Details and
129 historical results of FPI are in these references (Yuan et al., 2010; Wu et al., 2014; Yu et al., 2014; Huang et al., 2018; Jiang
130 et al., 2018).

131 2.4 Scattering radiative transfer model

132 The model for estimating scattering impact is based on the scattering radiative transfer model and numerical solution by
133 Harding (2017a). It assumes airglow emission undergoes elastic scattering, preserving its wavelength and initial Doppler shift.
134 By specifying airglow brightness distribution, original Doppler shift, lower atmosphere scattering characteristics, and a
135 simplified geometric relationship, the radiation transfer equations (see Appendix A) can be solved to compute the distribution
136 of multiple scattered light and its associated Doppler shift. This enables the wind simulation with atmospheric scattering. A
137 schematic diagram (Fig. 1) illustrates the basic mechanism. To enhance applicability, we have refined several aspects: (1) The
138 upper boundary of the lower atmosphere is set at 40 km to improve the accuracy of the effective extinction path in the initial
139 source function. (2) The LOS speed is used directly instead of the Doppler shift, assuming a constant background temperature.
140 (3) After binning different LOS speeds and computing the corresponding scattered light intensity, contaminated LOS speeds
141 are calculated via weighted average, simplifying the wind simulation. We directly use LOS speed instead of Doppler shift,
142 primarily neglecting the interference fringe recognition errors caused by spectral broadening due to temperature variations.
143 During auroral events, FPI observations show similar neutral temperatures in all directions, with the northward direction
144 occasionally being about 300 K higher (not shown here). Overall, the temperature at mid-latitudes is uniform at the 500 km
145 spatial scale, and the variations caused by spectral line broadening can be neglected. The detailed model description is provided
146 in Appendix A.

147 Additionally, the scattering characteristics of the lower atmosphere in our model, including the scattering phase function and
148 optical depth, were derived from Aerosol Robotic Network (AERONET) observations (Holben et al., 2001). We utilized data
149 from the Baotou site (40.9° N, 109.6° E), which is the nearest available site to SIZW, located approximately 180 km away.
150 The total optical depth, accounting for both aerosol and molecular scattering, was calculated using monthly averages and was
151 found to be 0.43 in May and 0.2 in October. The scattering phase function was determined based on AERONET data following
152 the previous method (Harding et al., 2017a). Further details regarding the scattering characteristics are described in Appendix
153 B.

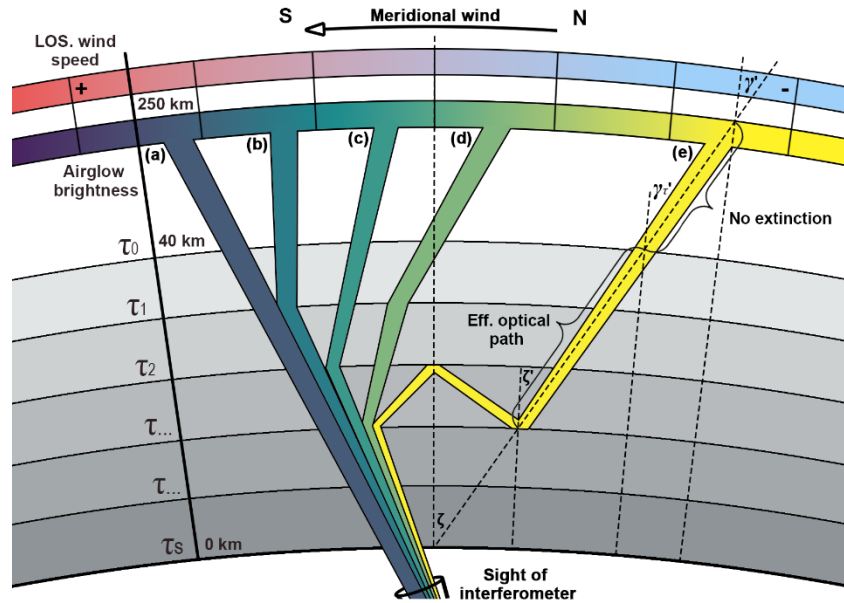


Figure 1: The schematic diagram of the scattering radiative transfer model

The grey shading represents the lower atmospheric layer, with darker hues indicating greater optical depth. The yellow-green fillers represent the relative brightness from the red-line airglow layer. Yellow indicates higher light intensity. The blue-red fillers, which correspond to the relative brightness, represent the Doppler shift type (blue-shift or red-shift) of LOS wind speeds. (a) to (e) represent airglow emissions travelling along different paths, carrying Doppler shifts from outside the line of sight into the interferometer, thereby causing biases in the observations. The model estimates the biases by simulating the distribution of airglow emissions after scattering.

3 Results

Two storms with visible auroras on May 10th and Oct. 10th, 2024, respectively, are used to study the scattering impact. The storm from May 10th to 11th is characterized by its significant magnitude and prolonged duration. Multiple works report this event (Guo et al., 2024; Hajra et al., 2024; Themens et al., 2024), with particular focus on the variations of thermospheric winds (Wang et al., 2025; Zhang et al., 2025) and auroras (Gonzalez-Esparza et al., 2024; Kataoka et al., 2024b; Mikhalev, 2024; Nanjo and Shiokawa, 2024) at mid-latitudes. The storm commenced around 17:00 UT on May 10th and the main phase persisted until 02:00 UT on May 11th. After that, the local night of May 11th in the China region sank into a continuous recovery phase. Another storm from Oct. 10th to 11th is weaker than May's (Ranjan and Pallamraju, 2025; Singh et al., 2025), with the main phase from 18:00 UT on Oct. 10th to 02:00 UT on Oct. 11th. During the two geomagnetic storms with visible auroras, both the DCOI and FPI at SIZW observed atypical winds, characterized by intense horizontal wind differences and downward vertical winds.



3.1 Storm-time wind speed statistics

It is necessary to ascertain whether atypical winds originate from atmospheric scattering with spatially uneven airglow brightness or dynamic processes during storms. To investigate the impact of visible auroras on atypical winds during storms, we made the most of the available observations, tracking DCOI's storm-time observations for nearly a year and FPI's for almost five months. We employed the planetary magnetic index K_p exceeding 3 to identify geomagnetic storms (Yang et al., 2020). Besides, to rule out moonlight and cloud effects, we only used clear sky conditions, which means: (1) excluding cases where the angle between the moon and the line of sight is less than 30 degrees, and (2) excluding cases where large-area thick cloud coverage is visible in DCAI. Additionally, data with standard errors greater than $50 \text{ m}\cdot\text{s}^{-1}$ were also excluded. A few aurora events, including Nov. 5th, Dec. 1st, 2023, and Aug. 12th, 2024, that did not meet this criterion were excluded.

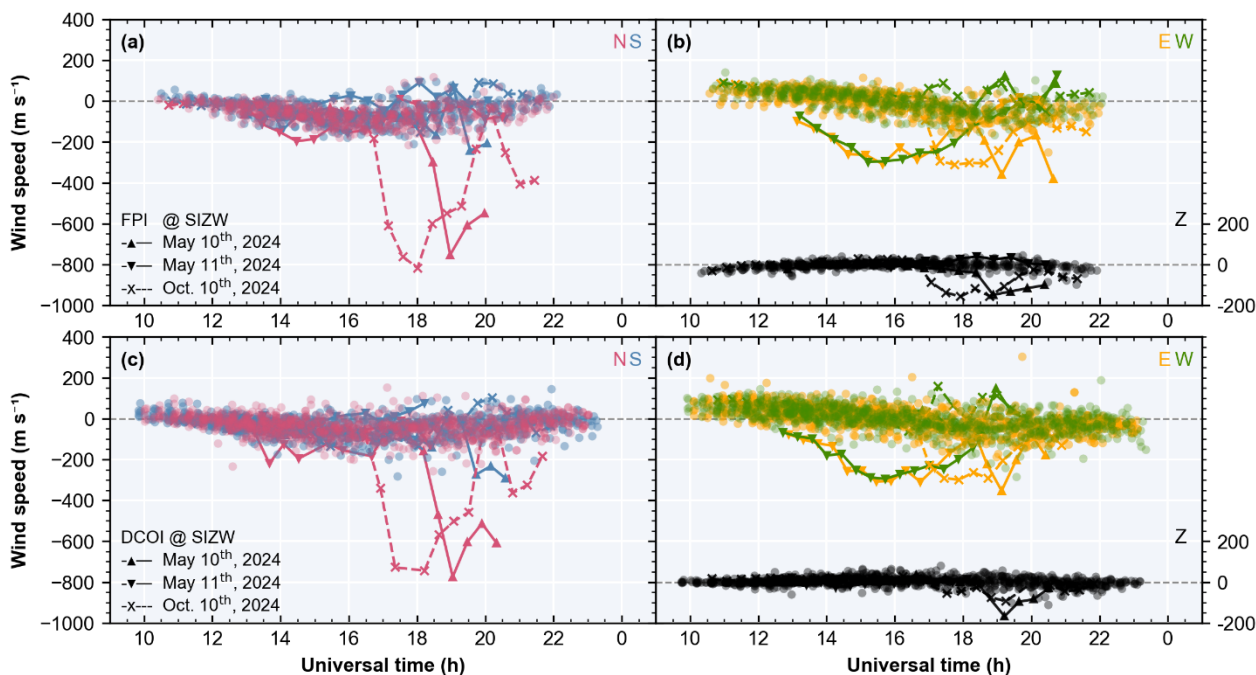


Figure 2: Storm-time ($K_p > 3$) thermospheric wind speed statistics at SIZW

Figure 2a shows meridional winds observed along two opposite directions (N-S) by FPI, with north-looking in red and south-looking in blue. Figure 2b shows zonal and vertical wind, with east-looking in yellow, west-looking in green, and zenith-ward in black. The northward, eastward, and upward speeds are positive in coordinates. Observations without aurora are shown as points, while those with visible auroras are shown as lines. Figures 2c and 2d are similar but show DCOI data.

Figure 2 shows thermospheric wind statistics during geomagnetic storms ($K_p > 3$) at SIZW. The first two panels display FPI data from May to Oct. 2024, while the rest display DCOI data from Nov. 2023 to Oct. 2024. FPI began operation on May 8th, 2024, with about half a year less data than DCOI. Observations with no aurora in the field of view are marked as points, while



the two cases with visible auroras are shown as lines. The five observation directions of the interferometer are marked by different colors. During typical storms, horizontal winds consistently increase to around $150 \text{ m}\cdot\text{s}^{-1}$ both equatorward and westward with no significant downward wind. However, under visible auroras, both DCOI and FPI have detected large wind speeds, such as a southward wind of about $600 \text{ m}\cdot\text{s}^{-1}$ and downwelling exceeding $100 \text{ m}\cdot\text{s}^{-1}$. The two series of winds observed along opposite cardinal directions (N-S or E-W) exhibit overt differences, with values exceeding $400 \text{ m}\cdot\text{s}^{-1}$ and contrary directions. This is markedly different from the wind patterns observed during non-aurora storms, where opposite-direction winds do not show significant divergence. Comparing the results of DCOI and FPI, the observations are largely consistent both with and without auroras. The atypical winds observed simultaneously by two interferometers with different principles suggest a systematic error from outside the instruments. Besides, these simultaneous changes appear in five observation directions, all characterized by enhanced negative LOS speeds, indicating likely LOS speed contamination. These factors point more towards scattering impact rather than dynamical processes as the cause. Next, the relationship between scattered light and atypical winds will be investigated through simulation.

3.2 Comparison of observations and simulations

Figure 3 shows the red-line airglow brightness from DCAI (Fig. 3a, 3e), the observed winds from DCOI and FPI (solid lines with different markers in Fig. 3b-3d, 3f-3h) and the simulated winds from the scattering model (dotted lines in Fig. 3b-3d, 3f-3h) during the two nights of May 10th and 11th, 2024, at SIZW, in which the different colors denote distinct directions. The grey lines in the horizontal wind plots represent the average values between opposite cardinal directions. The multi-directional brightness series from DCAI are extracted at 45° zenith angle, consistent with the scanning zenith angle of interferometers. Time intervals with visible auroras are highlighted in red, showing much higher brightness in northward directions than others. Figure 4 supplements the auroral distribution compared to Fig. 3a and 3e. Images from DCAI are projected onto the airglow layer at 250 km. The red circle encloses the actual observations with zenith angles less than 70° , while the values outside are extrapolated. The red dots represent the interferometer's pierce points on the airglow layer at 45° zenith angle.

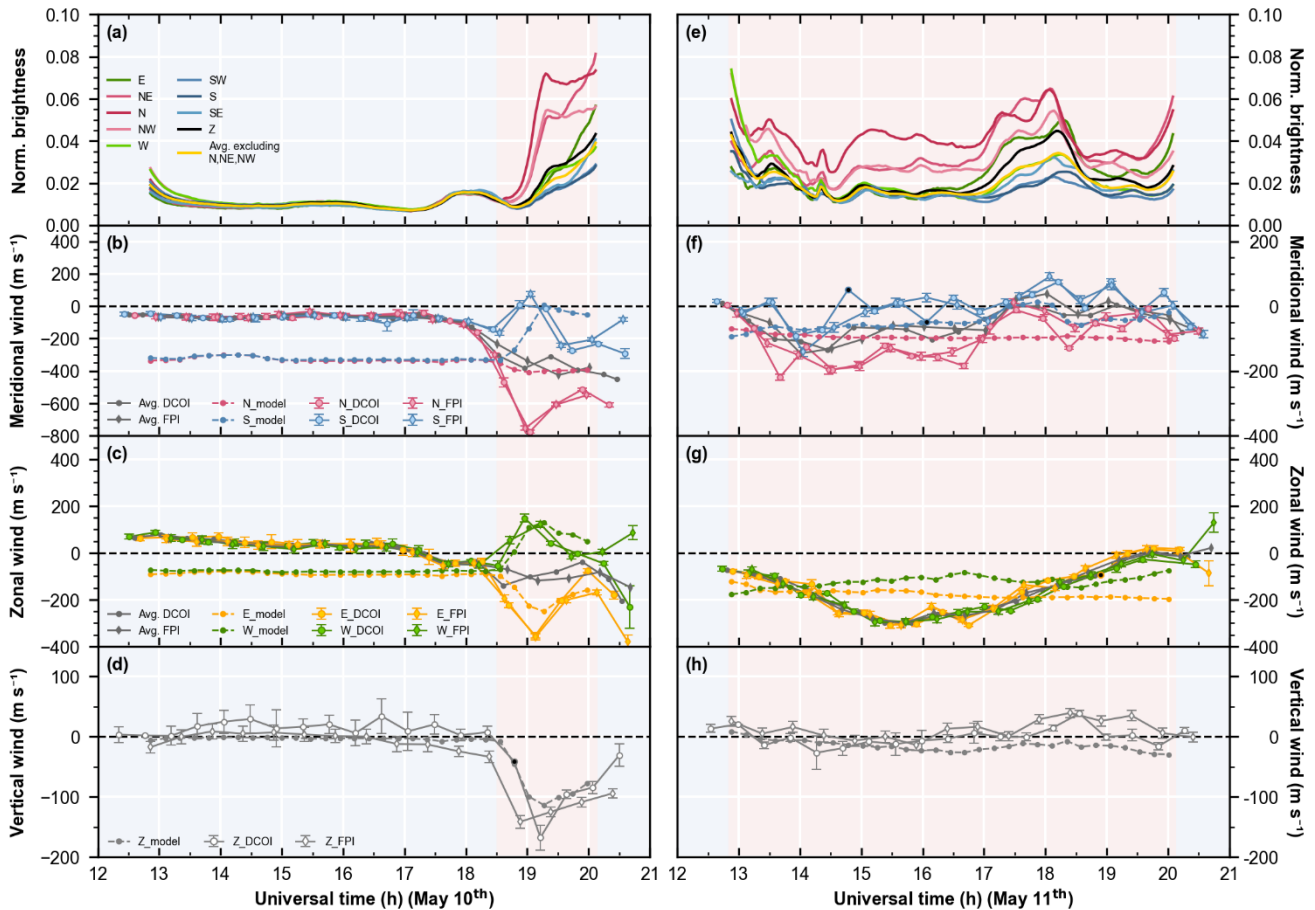


Figure 3: Observations of aurora and wind speeds, and the scattering model simulation on the nights of May 10th and 11th, 2024, at SIZW

Figure 3a shows the brightness of 8 cardinal directions, all at 45° zenith angle, along with the zenith-ward, extracted from DCAI. The color coding is as follows: red for northern directions, green for east and west, blue for southern directions, black for the zenith, and yellow for the average brightness excluding the three northern directions. Figure 3b shows the meridional wind, with north-looking in red and south-looking in blue, and the average of the two directions in grey. DCOI observations are shown as solid lines with circular dots, FPI as solid lines with rhombus dots, and simulations as dotted lines. Figures 3c, 3d are similar to Fig. 3b, but for zonal and vertical wind, with east-looking in yellow, west-looking in green, and zenith-ward in black. For a more concise figure, if the standard error exceeds 100 m·s⁻¹, the point will be filled with black instead of error bar. Figures 3a-3d show data from May 10th, and Fig. 3e-3h from May 11th. The time intervals with visible auroras are marked in red.

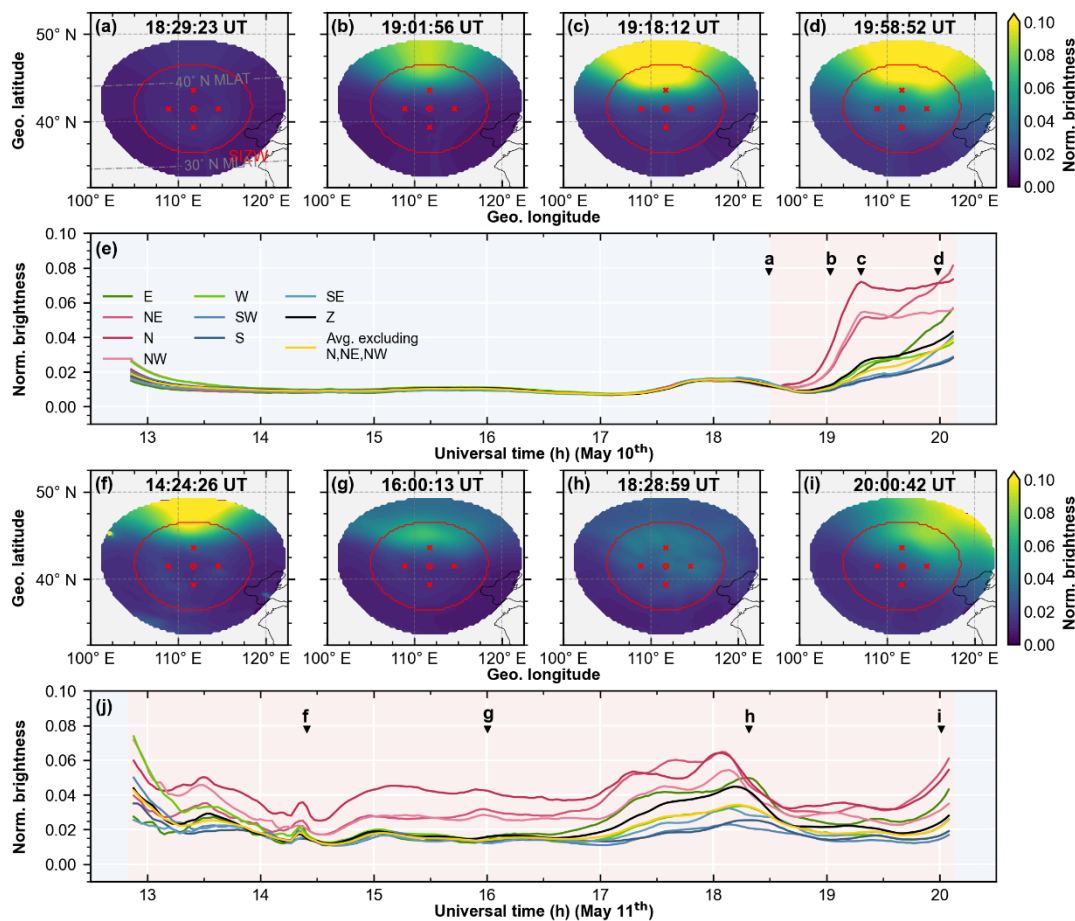


Figure 4: Auroral distribution observed by DCAI on the nights of May 10th and 11th, 2024, at SIZW

Images from DCAI (Fig. 4a-4d, 4f-4i) have been projected onto the airglow layer at 250 km. The red circle encloses actual observations with zenith angles $< 70^\circ$, while values outside are extrapolated using zero-order extrapolation. The red dots represent the interferometer's pierce points on the airglow layer at 45° zenith angle. Figures 4e, 4j are similar to Fig. 3a, 3e, with the corresponding images time labelled.

The coastlines in projected DCAI images are made with Natural Earth.

After 18:30 UT on May 10th, as the aurora intensified, both DCOI and FPI detected simultaneous changes in meridional, zonal, and vertical winds. The north-looking red-line brightness at 45° zenith angle exceeded three times that of other directions. The meridional and zonal wind differences between opposite cardinal directions (N-S or E-W) increased. And the winds detected in opposite directions reversed. The maximum meridional difference was close to $800 \text{ m}\cdot\text{s}^{-1}$, while that in zonal exceeded $500 \text{ m}\cdot\text{s}^{-1}$. The downward wind was enhanced by over $100 \text{ m}\cdot\text{s}^{-1}$. These four aforementioned variables, that red-line brightness, the meridional and zonal differences, and downwelling, increased almost simultaneously, peaked at 19:05 UT, and then decayed.



Moreover, the average meridional wind, derived from averaging opposite cardinal directions, continuously enhanced equatorward to around 400 m/s, while the average zonal wind enhanced westward to around 100 m/s. Unlike the single-direction results that peaked at 19:05 UT, the average wind varied steadily, consistent with storm-time circulation. Compared to the average wind, the separated horizontal and enhanced vertical winds are atypical. Even with travelling atmospheric disturbances (TADs) superimposed on storm-time circulation, phase lags between horizontal and vertical components would be expected (Hernandez and Roble, 1976; Ishii et al., 1999), but none were observed. Thus, the atypical winds do not appear to be the result of a dynamical process. During the recovery phase on May 11th, the aurora was present throughout the night but much weaker than on May 10th, as seen in Fig. 4. Both DCOI and FPI showed westward and equatorward horizontal winds with no significant downward wind. There was a meridional difference of about 100 to 300 m·s⁻¹ persisted throughout the night, with no zonal difference.

Subsequently, we used the scattering model to explore the relationship between red-line brightness variations and atypical winds through atmospheric scattering. On May 10th, a fixed wind vector of 100 m·s⁻¹ westward and 400 m·s⁻¹ southward was set as the input. This assumed wind was kept constant over time and spatially uniform, with no vertical components. On May 11th, a fixed wind vector of 200 m·s⁻¹ westward and 100 m·s⁻¹ southward was used, again with no vertical component. These values are chosen based on average observed wind speeds to approximate storm-time circulation. Although the specific values may deviate, the main wind directions remain consistent. The storm-time enhancement of vertical winds may be caused by scattering rather than representing real winds, so we set it to zero. It is worth noting that we neglect the variation of background wind in the model inputs, due to uncertainty regarding whether the observed wind variations are biased. Moreover, using fixed wind speeds allows us to highlight the impact of red-line brightness variations and determine the presence of scattering effects.

As the dotted lines in Fig. 3b-3e, the simulations with scattering impact generally match the observations on May 10th. Simulated horizontal wind differences and downwelling increase initially with the aurora, peak around 19:15 UT, and then decay. The simulated wind speed variations lag the observations by about 10 minutes. The lag may be due to the relatively rough 25 minute scanning cycle or DCAI underestimating airglow brightness at the field of view's edge, leading to inaccurate capture of scattering enhancement start time. Numerically, the simulated zonal and vertical winds match observations more closely than the meridional wind. The simulated meridional difference is smaller than the observed difference, and the north-looking simulation remains closer to the default value, unlike the equatorward-biased observation. The preset fixed wind may influence the meridional simulation, as it does not follow the equatorward enhancement of the meridional wind. Other factors beyond scattering impact might also have an impact, such as spectral pollution caused by auroras (Makela et al., 2014), to be discussed later. Additionally, the model simulates a similar intense downward wind as observed under the preset zero vertical wind. This indicates that the vertical wind is significantly affected by scattering. This is why the intense vertical wind is not subtracted when converting interferometer LOS speed to horizontal wind, to prevent error propagation. For May 11th, due to the weak but continuous aurora, the simulation shows weak horizontal differences and slight downward winds throughout the



267 night. Compared with the observations, the simulation shows smaller meridional differences. It also indicates zonal differences
268 and downward winds, which are not evident in the observations. The poorer simulation on May 11th may be due to
269 misalignment between dominant horizontal winds and airglow brightness gradients, which will be discussed later. Additionally,
270 there may be issues with the zero wind calibration. When auroras are present throughout the night, the vertical wind, which
271 includes scattering biases, may have been used to calibrate zero wind speed. It likely masks the scattering impact in the
272 observations and explains the discrepancies in the simulation.

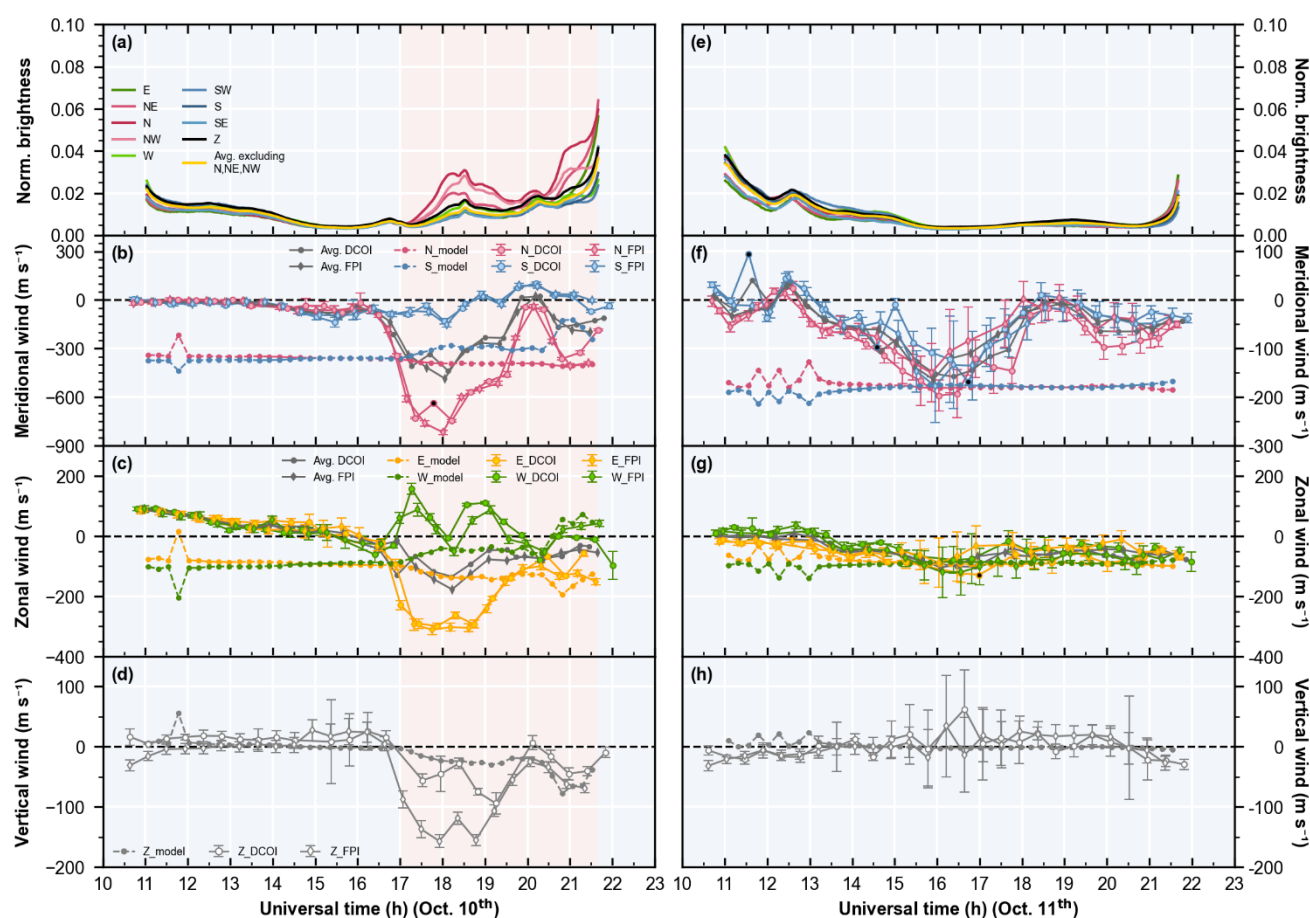


Figure 5: Observations of aurora and wind speeds, and the scattering model simulation on the nights of Oct. 10th and 11th, 2024, at SIZW

Figure 5 is analogous to Fig. 3, but for Oct. 10th and 11th.

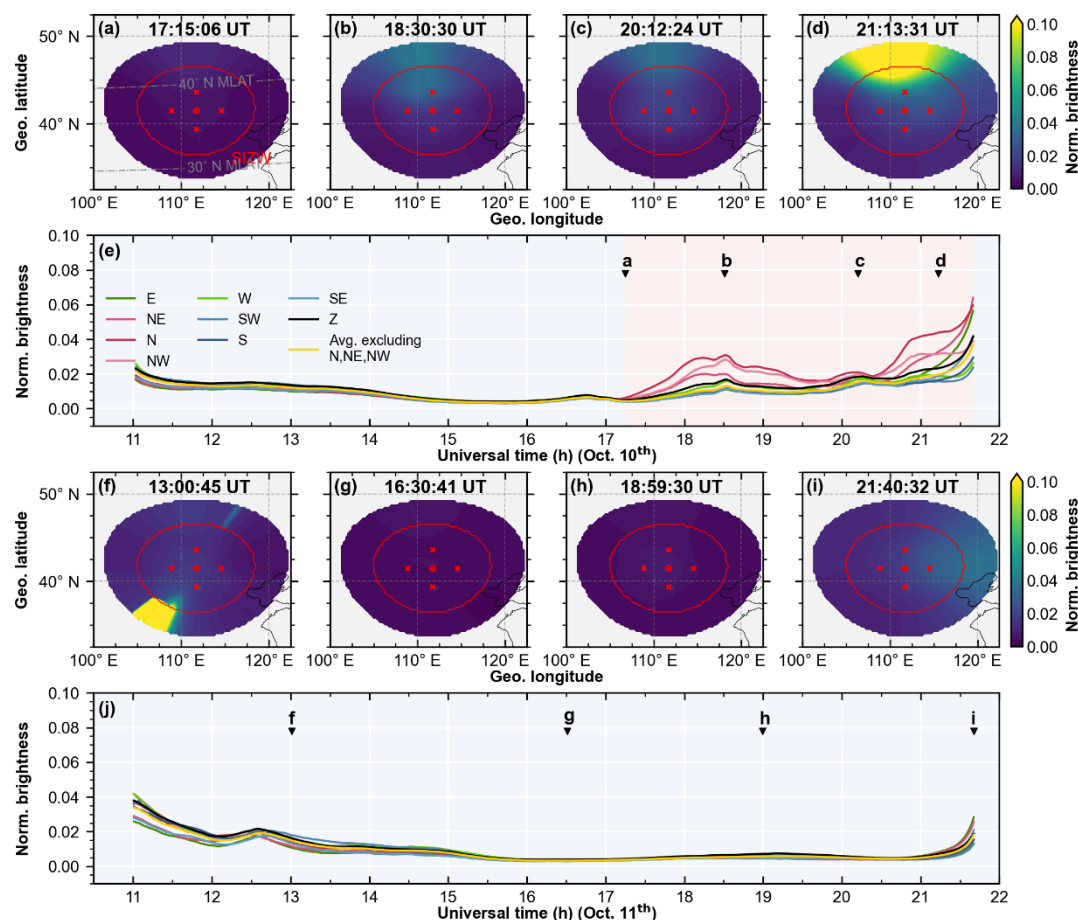


Figure 6: Auroral distribution observed by DCAI on the nights of Oct. 10th and 11th, 2024, at SIZW

Figure 6 is analogous to Fig. 4, but for Oct. 10th and 11th.

277

278

279

280 Figures 5 and 6 show another case from Oct. 10th to 11th, analogous to Figures 3 and 4. On Oct. 10th, the aurora appeared at
281 17:15 UT, expanded southward and increased in brightness, peaking first at 18:30 UT before decaying and then increasing
282 again from 20:30 UT until sunrise. The second peak was brighter than the first (Fig. 6). Similar to the storm in May, once
283 aurora appeared, both DCOI and FPI observed atypical winds, with synchronous meridional and zonal differences and
284 downward enhancements in vertical wind. These atypical winds also exhibited two peaks, around 18:30 UT and 21:00 UT.
285 The horizontal winds observed in opposite cardinal directions were basically in opposition. During visible aurora periods,
286 DCOI and FPI showed a 50 to 100 m·s⁻¹ difference in vertical wind but consistent variation trends. Moreover, the average
287 horizontal wind between opposite cardinal directions was dominantly equatorward and westward, which also had two peaks.
288 On Oct. 11th, the storm had passed, and no visible aurora was present. The increase in brightness around 13:00 UT was due to
289 moonset in the southwest. There were no significant horizontal differences or downward winds, consistent with geomagnetic
290 quiet conditions.



291 We set a fixed $100 \text{ m}\cdot\text{s}^{-1}$ westward with $400 \text{ m}\cdot\text{s}^{-1}$ southward wind vector for Oct. 10th, and $100 \text{ m}\cdot\text{s}^{-1}$ westward with $200 \text{ m}\cdot\text{s}^{-1}$
292 southward wind vector for Oct. 11th in the model, respectively, with no vertical component. The simulation on Oct. 10th exhibits
293 two peaks. The second peak in the simulation is consistent with the observations better, while the first peak, although capturing
294 the trend, is significantly underestimated in magnitude. This discrepancy in the simulation may relate to optical depth, aurora
295 brightness, and background wind changes. The optical depth in Oct. is about half that of May, and simulations underestimate
296 observed values. As in previous studies (Harding et al., 2017b), optical depth can affect the scattering model response. On Oct.
297 10th, the first aurora brightening is weaker than the second. When red-line brightness differences are small, the model response
298 tends to be lower. The impact of optical depth and red-line brightness on the model will be discussed later. Additionally,
299 noticeable fluctuations in the average meridional wind on this day may also contribute to the deviation in the model with fixed
300 initial wind. The north-looking wind speed varied dramatically between 19:00 UT and 21:00 UT along with the aurora, which
301 may also be related to spectral contamination beyond scattering impact. This spectral contamination arises from fast O atoms
302 generated by low-energy O^+ ion precipitation in the auroral region, which occurs at higher altitudes. This issue introduces an
303 additional spectral shift that compromises wind retrieval (Makela et al., 2014). This exceeds the simulation range of the model,
304 thereby causing the discrepancy.

305 4 Discussions

306 In this study, we modelled scattered airglow transmission in the lower atmosphere. Post-scattering wind speeds were calculated
307 based on initial wind speeds weighted by both scattered and direct intensities. The model basically captured the temporal
308 variations of horizontal wind differences and downward enhancements associated with varying auroral brightness, suggesting
309 the contribution of scattering mechanisms to atypical winds. However, the simulation of scattering has certain limitations and
310 characteristics: (1) The differences between simulation and observation vary across different directions. (2) The simulated
311 values sometimes exhibit significant numerical deviations from observations. Could this be related to model errors? (3) When
312 using average wind speeds and individual direction wind speeds with scattering impact, what additional considerations are
313 needed? Next, we will discuss these three issues in detail, focusing on the working principle of the model, the errors involved,
314 and the insights that the simulation can provide regarding the impact of scattering.

315 4.1 Core working principle of the scattering model

316 As shown in Fig. 3 and Fig. 5, observed winds respond differently to scattering across directions, especially on May 10th and
317 Oct. 10th with stronger auroras. Although the scattering model has numerical errors, the simulations also show directional
318 differences in scattering-induced biases. Both observations and simulations indicate that the meridional wind responds the
319 most, followed by the zonal wind, while the vertical wind responds the least. Since vertical and horizontal wind speeds are
320 derived from the projection of LOS wind speeds, this essentially reflects the non-uniform response of LOS speeds to scattering.
321 This directional inhomogeneity of scattering impact aligns with previous studies. Harding et al. (2017a) simulated scattering



322 effects under auroral conditions, using northward observations as the initial winds. They noted that this direction experiences
323 minimal scattering contamination due to facing the brighter region. Abreu et al. (1983) used a meridional one-dimensional
324 model, finding that LOS wind speeds near intense airglow brightness gradients and with weaker airglow intensity are more
325 susceptible to contamination. They also showed that scattering-induced biases are minimal in the vertical direction because
326 the light path through the atmosphere is shortest, reducing scattering opportunities. In this study, we further explore the
327 scattering impact as a function of azimuth angle, revealing the formation of horizontal differences.

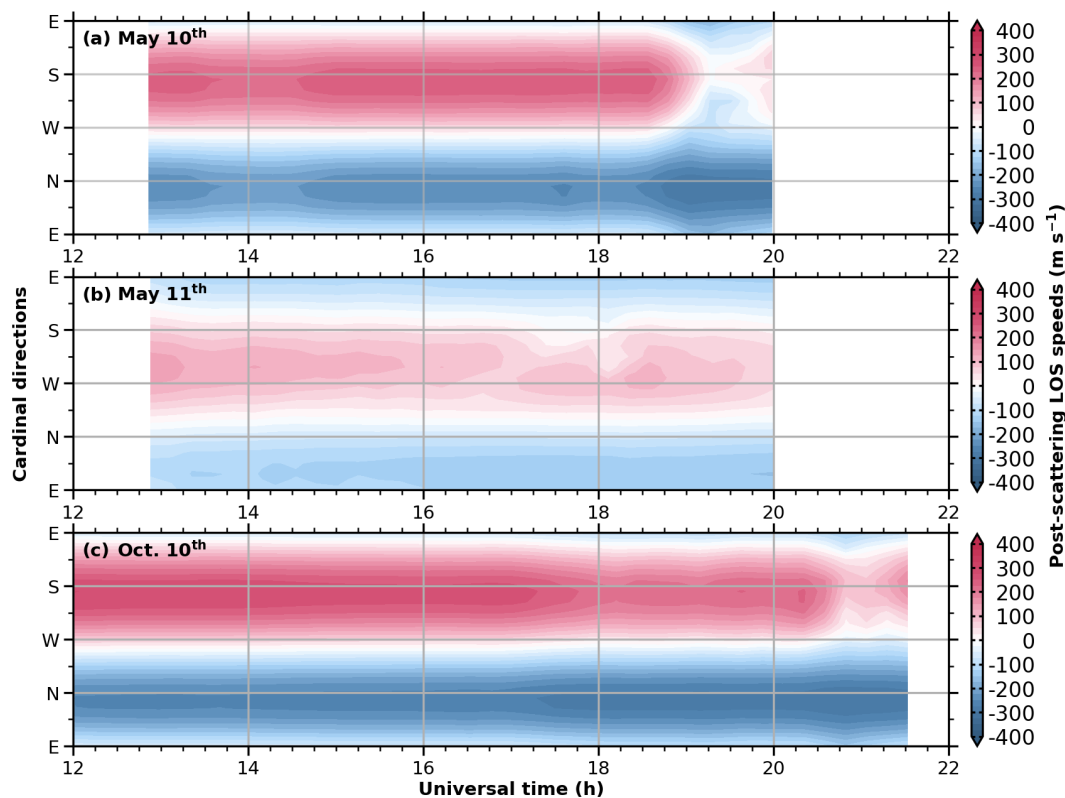


Figure 7: Post-scattering LOS speeds at 45° zenith angle

330 The figure shows the post-scattering line-of-sight speeds at 45° zenith angle for various directions over time, with panels for May 10th,
331 May 11th, and October 10th, respectively.

332 Figure 7 shows post-scattering LOS speeds at 45° zenith angle in the simulations on three aurora nights, with the vertical axis
333 indicating cardinal directions derived from azimuth angles. Concerning the auroral variations in Fig. 4 and Fig. 8, LOS speeds
334 show diffusion during auroral events. Negative LOS speeds initially concentrated northward, spread westward and eastward,
335 expanding horizontal coverage. Positive LOS speeds initially in the southward direction shrink. When converted to horizontal
336 wind speeds, these changes lead to increased horizontal differences, or the false convergence caused by scattering, in other



words. The northward LOS speed changes slightly, the southward speed changes the most and nearly reverses, while the eastward and westward speeds are intermediate.

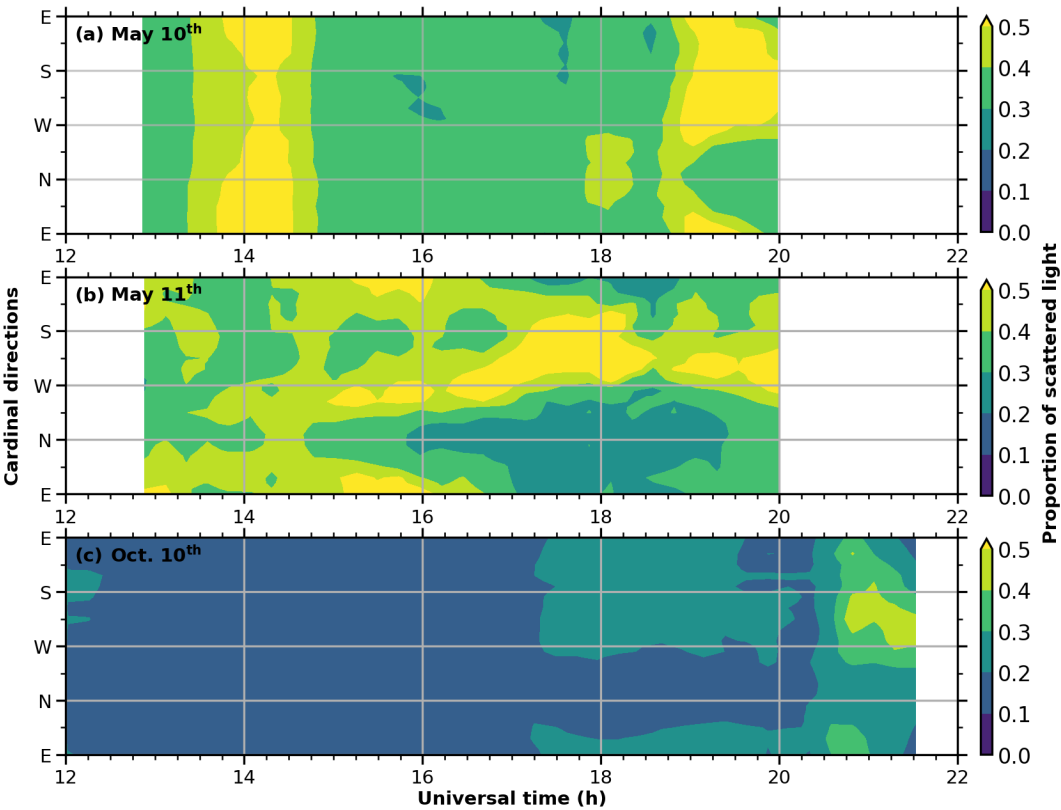


Figure 8: Proportion of scattered light at 45° zenith angle

The proportion is the ratio of scattered light intensity to the total light intensity (both scattered and direct) in the simulation. The figure shows this proportion at 45° zenith angle for various directions over time, with panels for May 10th, May 11th, and October 10th, respectively.

Figure 8 shows the ratio of scattered light intensity to total light intensity at a fixed 45° zenith angle calculated by the scattering model. Consistent with the schematic diagram (Fig. 1), the scattered intensity is the sum of all injected directions, and the total light intensity includes the direct component on this basis. Without auroras, the scattering proportion is typically below 0.4 and varies with atmospheric scattering capability. However, during auroral events, the scattering proportion in some directions can increase to 0.5 or higher. The northward scattering proportion increases the least and remains much lower than in other directions. In contrast, the scattering proportion is significantly enhanced in directions ranging from 135° to 180° away from northward. The aurora appears in the north, resulting in much higher northern brightness. After atmospheric scattering, light from the north diffuses into surrounding directions, increasing the scattering proportion. Because the north itself has strong



352 direct light, its scattering proportion remains small. In the model, we assume that without considering temperature-related
353 spectral broadening, stronger light rays dominate interference fringe identification (Wei et al., 2020), thereby determining the
354 Doppler shift or LOS speeds. The lower scattering proportion in the north allows northward observations to retain more LOS
355 speeds from themselves, while other directions experience greater LOS speed contamination from the north. Therefore, the
356 northward simulation is closest to the default inputs, the southward simulation deviates the most, and the eastward and
357 westward simulations lie in between. Additionally, the scattering impact should also consider the initial LOS speeds in the
358 brighter region. Despite the high scattering proportion on May 11th shown in Fig. 7, the simulated LOS speed changes in Fig.
359 8 are minimal. This is because of the smaller LOS speed in the auroral region on that day, resulting in less contamination
360 spread to other directions.

361 The core working principle of the scattering model relies on the relationship between airglow brightness and background LOS
362 wind speeds. As Harding (2017a) noted, scattering requires a bright sky region with large LOS wind speeds. Firstly, spatially
363 uneven airglow brightness is a prerequisite for significant scattering. The brightest airglow area contributes most to scattered
364 light intensity, and its Doppler shifts determine the LOS biases in other directions. This principle allows a rough assessment
365 of scattering impact without model computation when airglow is uneven. Locate the brightest region and its Doppler shift type,
366 as the same Doppler shift type will likely appear in other directions. Blue-shift dominance indicates increased downward wind
367 and horizontal deviations opposite to the line of sight, resembling convergence, while red-shift dominance resembles
368 divergence. Minimal scattering-induced biases occur if the scattering proportion is very low due to uniform airglow brightness,
369 or if the LOS velocity in the bright region is near zero (i.e., the wind speed is perpendicular to the line of sight). Previous
370 observations can be directly verified by this principle and are basically in line with it (Hernandez and Roble, 1976; Price et al.,
371 1995; Ishii et al., 1999; Ishii et al., 2001; Makela et al., 2014). Unfortunately, scattering impact can complicate dynamic
372 analysis. In polar regions, auroras are characterized by green-line emissions, and thermospheric winds are significantly
373 influenced by ion drag, where scattering effects may not be prominent. In contrast, mid-latitudes have mainly red-line auroras
374 with large-scale uniform circulation, making the scattering impact more pronounced and distinguishable.

375 4.2 Errors of the scattering model

376 The model also exhibits certain errors and limitations. Scattering-induced biases in observations have nearly similar
377 magnitudes on May 10th and Oct. 10th. However, with the same 100 m·s⁻¹ westward and 400 m·s⁻¹ southward wind input, the
378 scattering-induced biases in the May case are significantly larger in magnitude and closer to reality compared to October. In
379 Fig. 7, the simulated LOS speeds show a larger diffusion range for the May 10th case compared to October. In Fig. 8, the
380 scattering proportion for May 10th is consistently higher than that for October. We attribute this difference to the distinct optical
381 depths in the two months, which are 0.43 and 0.2, respectively. Optical depth reflects atmospheric extinction capability and is
382 mainly related to aerosol content (see Appendix B). It primarily affects the extinction process and influences the magnitude of
383 scattering-induced biases by altering the proportion of scattered light. When the optical depth is artificially increased to a



384 higher value, such as around 0.6, the model more closely matches the Oct. observations. We find that the model underestimates
385 scattering effects when the optical depth is low.

386 In the October 10th event, the simulated scattering-induced biases are inconsistent between the two auroral brightness peaks.
387 In Fig. 7, the LOS speed variation is larger during the second peak, and in Fig. 8, the scattering proportion is greater. This is
388 because the scattering proportion is susceptible to errors in scattered and direct light intensities. DCAI doesn't correct for
389 Rayleigh units, leading to significant errors in regions with large zenith angles. The model can't fully eliminate the stray light
390 caused by the glass dome when separating the initial direct and scattered light from DCAI images (Harding et al., 2017a),
391 resulting in errors. In our experiments, if the stray light effect isn't subtracted as described in Appendix B, the model becomes
392 more inert, resulting in a smaller simulated scattering proportion.

393 In our experiments, the scattering model consistently underestimates scattering impact compared to observations, despite
394 several applied enhancements: (1) A single-scattering albedo of 1 was used, ignoring absorption. (2) Stray light effects were
395 removed. (3) Attenuated airglow observations at the edge of DCAI images were extrapolated, enhancing edge scattering. (4)
396 Excessive edge extinction was reduced by correcting the extinction path geometry, increasing the scattered light intensity
397 integral. (5) Zero vertical wind was assumed when converting simulated LOS speeds to geographical wind speeds. Since the
398 integral only includes 10 optical depth layers, with each light ray scattering once per layer and extinguishing once between
399 layers, it may be too crude compared to the real path, underestimating the scattered light. Simply increasing the number of
400 optical depth layers is not effective. We think this may be related to the non-linear variation of atmospheric density with
401 altitude, where optical depth may not vary linearly with height, and the scattering phase function may also change with altitude.
402 To address this issue, future work should complete the DCAI correction. Additionally, introducing a model of optical depth
403 varying with altitude can increase the number of single-scattering nodes and ensure the geometric accuracy of the extinction
404 path, thereby improving the accuracy of scattered light intensity calculations.

405 Furthermore, these bright region observations do not necessarily correspond to the wind speeds of the red-line airglow layer.
406 They could also come from higher auroral layers and not even reflect the neutral thermospheric winds near 250 km (Makela
407 et al., 2014). In Fig. 3 and Fig. 5, the north-looking wind observations show unusually high wind speeds, which are significantly
408 different from the simulations. In particular, on October 10th, the north-looking wind speed varied dramatically with the
409 intensity of the northern aurora. During the two auroral peaks, the north-looking wind direction also reversed. The north-
410 looking wind speed changed more than the south-looking wind speed, inconsistent with the simulation characteristics. When
411 auroras occur, the north-looking wind speed in the bright region may be significantly higher than the average value over zenith
412 and distinct from regions outside the aurora. This could enhance scattering effects, which the model fails to simulate.



413 4.3 Scattering effects on thermospheric wind observation

414 Given the directional inhomogeneity of scattering impact, the reliability of the commonly utilized average wind and individual
415 direction wind observations needs to be considered. Wind speed detected from a less bright region is more doubtful, because
416 these regions are more polluted by scattered light. The average speed of opposite cardinal directions will maintain the correct
417 time-varying trend of the background thermospheric wind but may deviate in absolute value. Since the LOS speed deviations
418 caused by scattering in each direction have the same type, averaging can cancel out the scattering deviations between opposite
419 directions, making the average wind closer to the true background thermospheric wind. However, in directions with strong
420 light intensity gradients, such as north-south, the deviations in the two directions are different, and averaging will cause the
421 wind speed to deviate from the true value. Additionally, the wave-like structures appearing in each individual direction may
422 originate from changes in scattering effects caused by variations in auroral intensity, and whether they come from TADs needs
423 further verification. The wave-like structures superimposed on the average value may also have their amplitudes enhanced or
424 cancelled due to the directionality of scattering deviations, which similarly requires additional validation.

425 5 Conclusions

426 This study has further proved that lower atmospheric scattering can bias thermospheric wind observation on ground-based
427 optical interferometers. The light scattered from the non-line-of-sight directions of the scope will lead to additional LOS speeds
428 and appear as atypical horizontal differences and vertical wind at geographic coordinates. With a simplified scattering radiative
429 transfer model, we simulate the distribution of airglow intensity after the multiple scattering of the lower atmosphere and
430 estimate the wind observation bias under scattering impact via a weighted average method. Atypical winds under conditions
431 of spatially uneven airglow have been generally captured.

432 We have refined the scattering model in previous research to enhance its computational efficiency. Specifically, we simplified
433 the LOS wind speed simulation and introduced an upper limit for the lower atmosphere to improve the accuracy of the
434 extinction length calculation. The scattering impact can be directly estimated through the relationship between the bright
435 airglow region and the LOS wind speed. The brightest airglow region contributes most to the scattering impact, of which the
436 Doppler shift type determines the LOS biases in other directions. Due to the directional inhomogeneity of scattering effects,
437 we propose that in directions with strong light intensity gradients, such as north-south, the average wind speed of opposite
438 directions and its fluctuations may be biased. Although the observed winds are affected by scattering when airglow is uneven,
439 they still retain dynamic information, such as the average wind being close to the storm-time circulation. Unfortunately, we
440 lack alternative observational methods to verify the accuracy of the interferometer results. It deserves further study to the
441 extent of scattering impact with more cases and additional instrumental observations.



Limited by the accuracy of the model inputs, the scattering model can only simulate the wind features associated with scattering impact under clear sky conditions. It remains incapable of precisely picking out the speed alterations induced by scattering impact. Given that scattering significantly impacts observations during geomagnetic storms accompanied by auroras, it is necessary to quantify these biases to provide accurate data for dynamic studies. Therefore, future efforts can focus on refining the model and its inputs or statistically analyzing scattering biases under different airglow brightness distributions from various stations to gain a clearer understanding of the magnitude of scattering biases.

Appendix A

In the following appendices, we provide a concise description of the scattering model's operational principles, inputs, and modifications employed in our works. For more detailed solutions, please refer to the article by Harding et al. (Harding et al., 2017a).

Based on the radiation transfer theory, Hansen and Travis (1974) and Sobolev (1975) gave the multiple scattering solution. Harding (2017a) extended the initial source function $J_0(\tau, u, \phi)$ to airglow surface source, and corrected the missing normalization factor in the scattering phase function (Eq. (1) to Eq. (3)):

$$u \frac{dI(\tau, u, \phi)}{d\tau} = -I(\tau, u, \phi) + J(\tau, u, \phi) \quad (1)$$

$$J(\tau, u, \phi) = \frac{\omega}{4\pi} \int_0^{2\pi} \int_{-1}^1 P(u, u', \phi, \phi') I(\tau, u', \phi') du' d\phi' + J_0(\tau, u, \phi) \quad (2)$$

$$J_0(\tau, u, \phi) = \frac{\omega}{4\pi} \int_0^{2\pi} \int_0^1 P(u, u', \phi, \phi') \sec(\gamma') f(u', \phi') \exp[-\tau L(u')] du' d\phi' \quad (3)$$

$$L(u) = [(R_e + H_L) \cos(\gamma_\tau) - R_e u] H_L^{-1} \quad (4)$$

$$u = \cos(\zeta) \quad (5)$$

The equations are formulated within an improved local spherical coordinate system, including azimuth ϕ , zenith angle ζ which is represented in cosine form u , and vertical height which is expressed as optical depth τ .

In the case of scattering, as illustrated in Fig. 1, the light intensity along a line of sight, represented by $I(\tau, u, \phi)$, consists of two parts, the direct light (a in Fig. 1) from the same direction, and the aggregate of scattered light (b-e in Fig. 1) from other directions, which is represented by the source function $J(\tau, u, \phi)$. Based on the radiative transfer equation (Eq. (1)), at each optical depth layer, the scattered light intensity received from all directions will be integrated. Simultaneously, the original intensity in the line of sight will be added to the total scattered light. Besides, the extinction in the path will be calculated according to the optical depth.



There are two potential scattering paths in the lower atmosphere: single scattering (b, c in Fig. 1) and multiple scattering (d, e in Fig. 1). The model computes them sequentially via an iterative process. In the initial state, there is no light intensity in the lower atmosphere. Therefore, the single scattering will originate solely from the airglow layer, and the source function $J(\tau, u, \phi)$ will be equivalent to the initial source function $J_0(\tau, u, \phi)$ at this state. By solving Eq. (1), the model can obtain the single scattered intensity in each direction at every optical depth layer, which is the updated source function $J(\tau, u, \phi)$. Then, the multiple scattering can be calculated based on it. Typically, the total scattered intensity will remain relatively constant when accounting for the fourth scattering. By using this iteration, the scattered light and residual direct light in DCAI images can be effectively separated. The residual direct light will subsequently serve as the background intensity distribution for simulating speeds.

In the source function $J(\tau, u, \phi)$, the scattering phase function $P(u, u', \phi, \phi')$ quantifies the relative gain of an incident angle to an exit angle during the scattering process. The reference value is based on a unit-radius sphere, which necessitates the introduction of a factor $\frac{1}{4\pi}$. Furthermore, ω represents the single-scattering albedo, set as 1. The initial source function $J_0(\tau, u, \phi)$ is responsible for introducing the airglow distribution $f(u', \phi')$. Here, $\sec(\gamma')$ represents the secant of the zenith angle at the puncture point of the airglow layer, which helps eliminate the Van Rhijn effect. Additionally, the exponential term with base e is utilized to calculate the equivalent extinction length along an inclined path.

It is primarily the lower atmosphere that significantly scatters and absorbs light (He et al., 2021; Li et al., 2022). Therefore, when computing the extinction length, just employing the cosine of zenith angle u' will lead to an overestimation of the effective length, as illustrated on the right side of Fig. 1. To address it, we set an upper boundary H_L of the lower atmosphere at 40 km, assuming an optical depth of zero above this altitude. Using geometric relationships, an equivalent length factor $L(u)$ can be derived, where R_e means Earth radius, and γ_t represents the zenith angle at the penetration point of 40 km height. This value can be readily calculated by adjusting the target height of the formula for γ . Inside the lower atmosphere, we apply a thin-layer approximation, which also utilizes the geometric relationships at the upper boundary.

$$V = \frac{V_{dr}I_{dr} + \sum_k V_{sc}(k)I_{sc}(k)}{I_{dr} + \sum_k I_{sc}(k)} \quad (6)$$

After working out the background intensity distribution, we partition the LOS speeds at 250 km into several bins. Ignoring the background temperature gradient, LOS speeds can directly correspond to Doppler shifts to simplify the simulation of the Doppler distribution. As roughly illustrated in Fig. 1, all LOS speeds are categorized into $k=10$ bins valued from highest to lowest, assuming that the LOS speeds within each bin approximate their mean value V_{sc} . The scattered intensity distribution I_{sc} is computed by extracting the airglow brightness from the corresponding region of each bin. And, there will be no intensity from other areas during a single bin's computing. According to Eq. (6), the simulative LOS speed at a specific angle will be an averaged result, where the original speed V_{dr} is weighted by the direct light intensity I_{dr} , and the additional speed resulting



498 from scattering V_{sc} is weighted by the scattered light intensity I_{sc} . The model directly uses the average within DCOI's 9
499 degree field of view as simulated post-scattering LOS speed of interferometers, since DCOI and FPI haven't measured the
500 reception gain of light outside their fields of view. We find that due to the coarse model grid, the 9 degree average is nearly
501 the same as using the nearest single-sight observation. Finally, the LOS speed will be converted to horizontal wind, maintaining
502 the assumption of zero vertical wind to prevent the propagation of scattering biases in the vertical direction.

503 **Appendix B**

504 This appendix details the scattering model's inputs from measurements, supplementing the second section. The background
505 airglow brightness for the model comes from DCAI. Image processing includes: (1) dark field exclusion, (2) median filtering
506 to remove starlight, (3) conversion to the local spherical coordinate, (4) stray light correction, (5) radial zero-order
507 extrapolation for regions beyond 70° zenith angle. Stray light results from the scattering of strong incident light by the glass
508 dome. During quiet nights without auroras, it is weak and uniformly distributed across all LOS directions. We use the azimuthal
509 average of the nearest quiet night at 45° zenith angle as a reference for weak stray light condition. After aurora onset, stray
510 light brightens all directions. The difference between the darkest direction at 45° zenith angle and the reference value is
511 considered the additional stray light caused by the aurora and is subtracted from the entire image. The shown airglow images
512 additionally mitigate the Van Rhijn effect through $\sec(\gamma')$ and the atmospheric extinction through $\exp[-\tau L(u')]$ (see
513 Appendix A). Since the scattering model already includes these processes, no separate treatment is needed. The optical depth
514 and scattering phase function inputs are shown in Fig. 9. Optical depth is calculated using AERONET's monthly averages,
515 with interpolation at 630 nm. Since only daytime observations are available, local daytime values are used to represent
516 nighttime values. Fig. 9a and 9b show monthly average optical depths at local daytime, with total averages of 0.43 and 0.2.
517 The scattering phase function is a weighted average of molecular and aerosol scattering phase functions from AERONET at
518 675 nm, which is weighted on the total optical depth of aerosols and molecules.

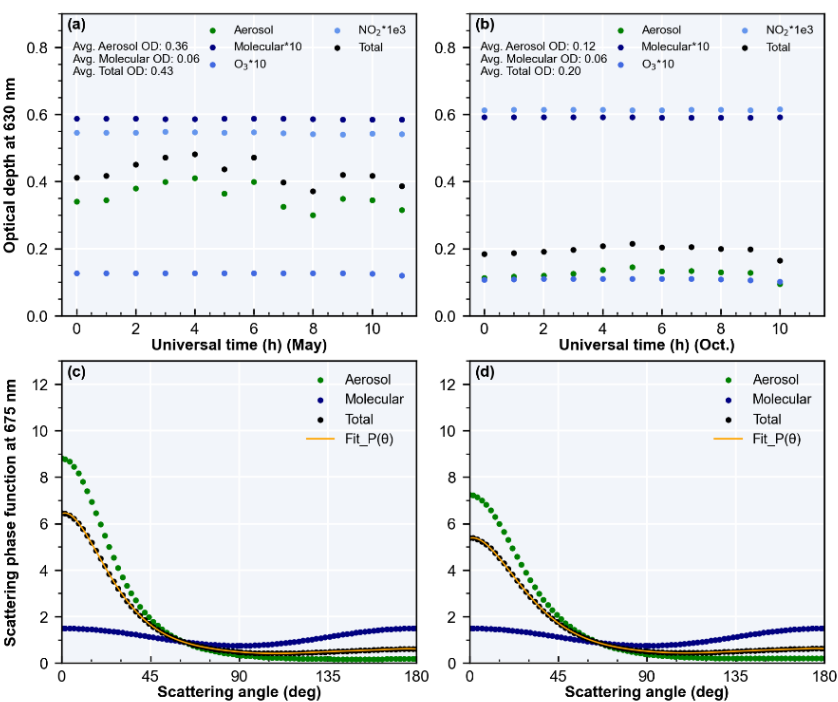


Figure 9: Optical depth and scattering phase function in May and October

The first two panels show daytime monthly average optical depths, with molecular optical depth amplified for clarity. The rest panels show the scattering phase functions.

Code availability

The code of DCAI images correction, the scattering model, and the visualization are not publicly available yet. If needed, they can be obtained by contacting the corresponding authors via email.

Data availability

The data of DCOI and DCAI from the Chinese Meridian Project can be obtained from <https://www.meridianproject.ac.cn/en/>. The FPI data can be obtained by contacting the corresponding authors via email. The data of AERONET can be obtained from <https://aeronet.gsfc.nasa.gov/>. The Kp index provided by GFZ, German Research Centre for Geosciences, can be obtained from <https://kp.gfz-potsdam.de/en/>.



531 **Author contributions**

532 Conceptualization: XW; investigation: XW, GJ; instruments construction and maintenance: YZ, JX, WL, TW, GZ, WY; wind
533 data retrieval: YZ, WL, GZ, TW; airglow images correction: XW; model improvement and programming: XW; visualization:
534 XW; validation: GJ, YZ, JX, WL, TW; writing - original draft preparation: XW; writing-review and editing: GJ, YZ, JX, WL,
535 TW; supervision: GJ, YZ; project administration: GJ, YZ; funding acquisition: YZ. All authors contributed to the revision and
536 improvement of the paper.

537 **Competing interests**

538 The authors declare that they have no conflict of interest.

539 **Acknowledgements**

540 We appreciate all the funding from the National Key R&D program of China (2023YFB3905100), the Project of Stable Support
541 for Youth Team in Basic Research Field, CAS (YSBR-018), the National Natural Science Foundation of China (42174212),
542 the Chinese Meridian Project, and the Specialized Research Fund for State Key Laboratories. We acknowledge the use of data
543 from the Chinese Meridian Project. We thank all the builders and maintainers of DCOI, FPI, and DCAI of Siziwang station.
544 We thank Lingli Tang for their effort in establishing and maintaining AOE_Baotou site of AERONET.

545 **Financial support**

546 This work was supported by the National Key R&D program of China (2023YFB3905100), the Project of Stable Support for
547 Youth Team in Basic Research Field, CAS (YSBR-018), the National Natural Science Foundation of China (42174212), the
548 Chinese Meridian Project, and the Specialized Research Fund for State Key Laboratories.

549 **References**

- 550 Abreu, V. J., Schmitt, G. A., Hays, P. B., Meriwether, J. W., Tepley, C. A., and Cogger, L. L.: Atmospheric Scattering Effects
551 on Ground-Based Measurements of Thermospheric Winds, *Planet Space Sci*, 31, 303-310, doi:10.1016/0032-
552 0633(83)90080-6, 1983.
- 553 Anderson, C., Conde, M., and McHarg, M. G.: Neutral thermospheric dynamics observed with two scanning Doppler imagers:
554 2. Vertical winds, *Journal of Geophysical Research: Space Physics*, 117, doi:10.1029/2011ja017157, 2012.
- 555 Ashburn, E. V.: The Effect of Rayleigh Scattering and Ground Reflection Upon the Determination of the Height of the Night
556 Airglow, *J Atmos Terr Phys*, 5, 83-91, doi:10.1016/0021-9169(54)90012-4, 1954.
- 557 Biondi, M. A. and Feibelman, W. A.: Twilight and nightglow spectral line shapes of oxygen $\lambda 6300$ and $\lambda 5577$ radiation, *Planet*
558 *Space Sci*, 16, 431-443, doi:10.1016/0032-0633(68)90158-X, 1968.
- 559 Biondi, M. A., Sipler, D. P., Zipf, M. E., and Baumgardner, J. L.: All-Sky Doppler Interferometer for Thermospheric Dynamics
560 Studies, *Appl Optics*, 34, 1646-1654, doi:10.1364/Ao.34.001646, 1995.



- 561 Burnside, R. G., Herrero, F. A., Meriwether, J. W., and Walker, J. C. G.: Optical observations of thermospheric dynamics at
562 Arecibo, *Journal of Geophysical Research: Space Physics*, 86, 5532-5540, doi:10.1029/JA086iA07p05532, 1981.
- 563 Burnside, R. G. and Tepley, C. A.: Optical Observations of Thermospheric Neutral Winds at Arecibo between 1980 and 1987,
564 *J Geophys Res-Space*, 94, 2711-2716, doi:10.1029/JA094iA03p02711, 1989.
- 565 Conde, M. and Smith, R. W.: Mapping Thermospheric Winds in the Auroral-Zone, *Geophysical Research Letters*, 22, 3019-
566 3022, doi:10.1029/95gl02437, 1995.
- 567 Conde, M., Craven, J. D., Immel, T., Hoch, E., Stenbaek-Nielsen, H., Hallinan, T., Smith, R. W., Olson, J., Sun, W., Frank, L.
568 A., and Sigwarth, J.: Assimilated observations of thermospheric winds, the aurora, and ionospheric currents over Alaska,
569 *Journal of Geophysical Research: Space Physics*, 106, 10493-10508, doi:10.1029/2000ja000135, 2001.
- 570 Crickmore, R. I., Dudeney, J. R., and Rodger, A. S.: Vertical Thermospheric Winds at the Equatorward Edge of the Auroral
571 Oval, *J Atmos Terr Phys*, 53, 485-492, doi:10.1016/0021-9169(91)90076-J, 1991.
- 572 Dhadly, M., Emmert, J., Drob, D., Conde, M., Doornbos, E., Shepherd, G., Makela, J., Wu, Q., Niciejewski, R., and Ridley,
573 A.: Seasonal dependence of northern high-latitude upper thermospheric winds: A quiet time climatological study based
574 on ground-based and space-based measurements, *Journal of Geophysical Research: Space Physics*, 122, 2619-2644,
575 doi:10.1002/2016JA023688, 2017.
- 576 Emmert, J. T., Fejer, B. G., Fesen, C. G., Shepherd, G. G., and Solheim, B. H.: Climatology of middle- and low-latitude
577 daytime region disturbance neutral winds measured by Wind Imaging Interferometer (WINDII), *J Geophys Res-Space*,
578 106, 24701-24712, doi:10.1029/2000ja000372, 2001.
- 579 Emmert, J. T., Faivre, M. L., Hernandez, G., Jarvis, M. J., Meriwether, J. W., Niciejewski, R. J., Sipler, D. P., and Tepley, C.
580 A.: Climatologies of nighttime upper thermospheric winds measured by ground-based Fabry-Perot interferometers during
581 geomagnetically quiet conditions: 1. Local time, latitudinal, seasonal, and solar cycle dependence, *J Geophys Res-Space*,
582 111, Artn A12302, doi:10.1029/2006ja011948, 2006.
- 583 Englert, C. R., Babcock, D. D., and Harlander, J. M.: Doppler asymmetric spatial heterodyne spectroscopy (DASH): concept
584 and experimental demonstration, *Appl Optics*, 46, 7297-7307, doi:10.1364/Ao.46.007297, 2007.
- 585 Englert, C. R., Harlander, J. M., Emmert, J. T., Babcock, D. D., and Roesler, F. L.: Initial ground-based thermospheric wind
586 measurements using Doppler asymmetric spatial heterodyne spectroscopy (DASH), *Optics Express*, 18, 27416-27430,
587 doi:10.1364/Oe.18.027416, 2010.
- 588 Fejer, B. G., Emmert, J. T., and Sipler, D. P.: Climatology and storm time dependence of nighttime thermospheric neutral
589 winds over Millstone Hill, *Journal of Geophysical Research: Space Physics*, 107, doi:10.1029/2001ja000300, 2002.
- 590 Friedman, J. F. and Herrero, F. A.: Fabry-Perot interferometer measurements of thermospheric neutral wind gradients and
591 reversals at Arecibo, *Geophysical Research Letters*, 9, 785-788, doi:10.1029/GL009i007p00785, 1982.
- 592 Gonzalez-Esparza, J. A., Sanchez-Garcia, E., Sergeeva, M., Corona-Romero, P., Gonzalez-Mendez, L. X., Valdes-Galicia, J.
593 F., Aguilar-Rodriguez, E., Rodriguez-Martinez, M., Ramirez-Pacheco, C., Castellanos, C. I., Pazos, M., Mendoza, B.,
594 Gatica-Acevedo, V. J., Melgarejo-Morales, A., Caraballo, R., Andrade-Mascote, E., Villanueva-Hernandez, P., Bonifaz-
595 Alfonso, R., Sierra, P., Romero-Hernandez, E., Peralta-Mendoza, I., Perez-Tijerina, E., Mejia-Ambriz, J. C., Guerrero-
596 Peña, C., Caccavari, A., Cifuentes-Nava, G., and Hernandez-Quintero, E.: The Mother's Day Geomagnetic Storm on 10
597 May 2024: Aurora Observations and Low Latitude Space Weather Effects in Mexico, *Space Weather-the International*
598 *Journal of Research and Applications*, 22, ARTN e2024SW004111, doi:10.1029/2024SW004111, 2024.
- 599 Guo, W. and McEwen, D. J.: Vertical winds in the central polar cap, *Geophysical Research Letters*, 30, Artn 1725,
600 doi:10.1029/2003gl017124, 2003.
- 601 Guo, X., Zhao, B. Q., Yu, T. T., Hao, H. L., Sun, W. J., Wang, G. J., He, M. S., Mao, T., Li, G. Z., and Ren, Z. P.: East-West
602 Difference in the Ionospheric Response During the Recovery Phase of May 2024 Super Geomagnetic Storm Over the
603 East Asian, *J Geophys Res-Space*, 129, ARTN e2024JA033170, doi:10.1029/2024JA033170, 2024.
- 604 Hajra, R., Tsurutani, B. T., Lakhina, G. S., Lu, Q. M., and Du, A. M.: Interplanetary Causes and Impacts of the 2024 May
605 Superstorm on the Geosphere: An Overview, *Astrophys J*, 974, ARTN 264, doi:10.3847/1538-4357/ad7462, 2024.
- 606 Hansen, J. E. and Travis, L. D.: Light-Scattering in Planetary Atmospheres, *Space Science Reviews*, 16, 527-610, doi:
607 10.1007/Bf00168069, 1974.
- 608 Harding, B. J., Makela, J. J., Qin, J., Fisher, D. J., Martinis, C. R., Noto, J., and Wrasse, C. M.: Atmospheric scattering effects
609 on ground-based measurements of thermospheric vertical wind, horizontal wind, and temperature, *Journal of Geophysical*
610 *Research: Space Physics*, 122, 7654-7669, doi:10.1002/2017JA023942, 2017a.



- Harding, B. J., Qin, J., and Makela, J. J.: Ground-Based Optical Measurements of Quiet Time Thermospheric Wind and Temperature: Atmospheric Scattering Corrections, *Journal of Geophysical Research: Space Physics*, 122, doi:10.1002/2017JA024705, 2017b.
- Harlander, J. M., Englert, C. R., Brown, C. M., Marr, K. D., Miller, I. J., Zastera, V., Bach, B. W., and Mende, S. B.: Michelson Interferometer for Global High-Resolution Thermospheric Imaging (MIGHTI): Monolithic Interferometer Design and Test, *Space Science Reviews*, 212, 601-613, doi:10.1007/s11214-017-0374-4, 2017.
- Hays, P. B., Killeen, T. L., Spencer, N. W., Wharton, L. E., Roble, R. G., Emery, B. A., Fullerrowell, T. J., Rees, D., Frank, L. A., and Craven, J. D.: Observations of the Dynamics of the Polar Thermosphere, *J Geophys Res-Space*, 89, 5597-5612, doi:10.1029/JA089iA07p05597, 1984.
- He, Q. F., Fang, Z., Shoshanim, O., Brown, S. S., and Rudich, Y.: Scattering and absorption cross sections of atmospheric gases in the ultraviolet-visible wavelength range (307-725 nm), *Atmos Chem Phys*, 21, 14927-14940, doi:10.5194/acp-21-14927-2021, 2021.
- Hernandez, G. and Roble, R. G.: Direct Measurements of Nighttime Thermospheric Winds and Temperatures .2. Geomagnetic Storms, *J Geophys Res-Space*, 81, 5173-5181, doi:10.1029/JA081i028p05173, 1976.
- Holben, B. N., Tanré, D., Smirnov, A., Eck, T. F., Slutsker, I., Abuhassan, N., Newcomb, W. W., Schafer, J. S., Chatenet, B., Lavenu, F., Kaufman, Y. J., Castle, J. V., Setzer, A., Markham, B., Clark, D., Frouin, R., Halthore, R., Karnieli, A., O'Neill, N. T., Pietras, C., Pinker, R. T., Voss, K., and Zibordi, G.: An emerging ground-based aerosol climatology:: Aerosol optical depth from AERONET, *J Geophys Res-Atmos*, 106, 12067-12097, doi:10.1029/2001jd900014, 2001.
- Huang, C., Xu, J. Y., Zhang, X. X., Liu, D. D., Yuan, W., and Jiang, G. Y.: Mid-latitude thermospheric wind changes during the St. Patrick's Day storm of 2015 observed by two Fabry-Perot interferometers in China, *Advances in Space Research*, 61, 1873-1879, doi:10.1016/j.asr.2017.10.013, 2018.
- Innis, J. L., Greet, P. A., Murphy, D. J., Conde, M. G., and Dyson, P. L.: A large vertical wind in the thermosphere at the auroral oval/polar cap boundary seen simultaneously from Mawson and Davis, Antarctica, *J Atmos Sol-Terr Phy*, 61, 1047-1058, doi:10.1016/S1364-6826(99)00060-7, 1999.
- Ishii, M., Oyama, S., Nozawa, S., Fujii, R., Sagawa, E., Watari, S., and Shinagawa, H.: Dynamics of Neutral Wind in the polar region observed with two Fabry-Perot interferometers, *Earth Planets Space*, 51, 833-844, doi:10.1186/Bf03353242, 1999.
- Ishii, M., Conde, M., Smith, R. W., Krynicki, M., Sagawa, E., and Watari, S.: Vertical wind observations with two Fabry-Perot interferometers at Poker Flat, Alaska, *Journal of Geophysical Research: Space Physics*, 106, 10537-10551, doi:10.1029/2000JA900148, 2001.
- Jiang, G., Xu, J., Wang, W., Yuan, W., Zhang, S., Yu, T., Zhang, X., Huang, C., Kerr, R. B., Noto, J., Li, J., Liu, W., and Li, Q.: A Comparison of Quiet Time Thermospheric Winds Between FPI Observations and Model Calculations, *Journal of Geophysical Research: Space Physics*, 123, 7789-7805, doi:10.1029/2018JA025424, 2018.
- Kataoka, R., Miyoshi, Y., Shiokawa, K., Nishitani, N., Keika, K., Amano, T., and Seki, K.: Magnetic Storm-Time Red Aurora as Seen From Hokkaido, Japan on 1 December 2023 Associated With High-Density Solar Wind, *Geophysical Research Letters*, 51, e2024GL108778, doi:10.1029/2024GL108778, 2024a.
- Kataoka, R., Reddy, S. A., Nakano, S., Pettit, J., and Nakamura, Y.: Extended magenta aurora as revealed by citizen science, *Scientific Reports*, 14, 25849, doi:10.1038/s41598-024-75184-9, 2024b.
- Killeen, T. L., Won, Y. I., Niciejewski, R. J., and Burns, A. G.: Upper Thermosphere Winds and Temperatures in the Geomagnetic Polar-Cap - Solar-Cycle, Geomagnetic-Activity, and Interplanetary Magnetic-Field Dependencies, *J Geophys Res-Space*, 100, 21327-21342, doi:10.1029/95ja01208, 1995.
- Li, J., Carlson, B. E., Yung, Y. L., Lv, D. R., Hansen, J., Penner, J. E., Liao, H., Ramaswamy, Kahn, R. A., Zhang, P., Dubovik, O., Ding, A. J., Lacis, A. A., Zhang, L., and Dong, Y. M.: Scattering and absorbing aerosols in the climate system, *Nat Rev Earth Env*, 3, 363-379, doi:10.1038/s43017-022-00296-7, 2022.
- Li, W. B., Liu, L. B., Chen, Y. D., Yang, Y. Y., Han, T. W., Ding, F., Le, H. J., and Zhang, R. L.: Multi-Instruments Observation of Ionospheric-Thermospheric Dynamic Coupling Over Mohe (53.5°N, 122.3°E) During the April 2023 Geomagnetic Storm, *J Geophys Res-Space*, 128, ARTN e2023JA032141, doi:10.1029/2023JA032141, 2023.
- Liu, W. J., Zhu, Y. J., Xu, J. Y., Li, Q. Z., Yuan, W., Zhu, G. Y., Wang, T. C., Yang, G. T., Du, L. F., Liu, S. Y., and Li, F. Q.: Validation of Neutral Wind in the Mesopause Measured by a Dual-Channel Optical Interferometer (DCOI) Network of the Chinese Meridian Project, *Space Weather-the International Journal of Research and Applications*, 23, ARTN e2025SW004468, doi:10.1029/2025SW004468, 2025.



- 661 Ma, L. X., Yu, Y. Q., Ding, X. Q., Liu, X. Y., An, D. P., Zhou, C. L., Cao, J. B., and Shiokawa, K.: Mid-Latitude Auroras and
662 Energetic Particle Precipitation Occurred Unusually in a Moderate Magnetic Storm on 1 December 2023, *Geophysical*
663 *Research Letters*, 51, ARTN e2024GL110764, doi:10.1029/2024GL110764, 2024.
- 664 Makela, J. J., Harding, B. J., Meriwether, J. W., Mesquita, R., Sanders, S., Ridley, A. J., Castellez, M. W., Ciocca, M., Earle,
665 G. D., Frissell, N. A., Hampton, D. L., Gerrard, A. J., Noto, J., and Martinis, C. R.: Storm time response of the midlatitude
666 thermosphere: Observations from a network of Fabry-Perot interferometers, *Journal of Geophysical Research: Space*
667 *Physics*, 119, 6758-6773, doi:10.1002/2014JA019832, 2014.
- 668 Mikhalev, A.: Auroras during extreme geomagnetic storms: Some features of mid-latitude aurora on February 11, 1958, *Solar-*
669 *Terrestrial Physics*, 55-61, 10.12737/stp-102202406, 2024.
- 670 Nakajima, H., Okano, S., Fukunishi, H., and Ono, T.: Observations of thermospheric wind velocities and temperatures by the
671 use of a Fabry-Perot Doppler imaging system at Syowa Station, Antarctica, *Appl Optics*, 34, 8382-8395,
672 doi:10.1364/Ao.34.008382, 1995.
- 673 Nanjo, S. and Shiokawa, K.: Spatial structures of blue low-latitude aurora observed from Japan during the extreme geomagnetic
674 storm of May 2024, *Earth Planets Space*, 76, ARTN 156, doi:10.1186/s40623-024-02090-9, 2024.
- 675 Price, G. D., Smith, R. W., and Hernandez, G.: Simultaneous Measurements of Large Vertical Winds in the Upper and Lower
676 Thermosphere, *J Atmos Terr Phys*, 57, 631-643, doi:10.1016/0021-9169(94)00103-U, 1995.
- 677 Ranjan, A. K. and Pallamraju, D.: Latitudinal Distribution of Thermospheric Nitric Oxide (NO) Infrared Radiative Cooling
678 During May and October 2024 Geomagnetic Storms, *J Geophys Res-Space*, 130, ARTN e2024JA033559,
679 doi:10.1029/2024JA033559, 2025.
- 680 Rees, D., Smith, M. F., and Gordon, R.: The Generation of Vertical Thermospheric Winds and Gravity-Waves at Auroral
681 Latitudes .2. Theory and Numerical Modeling of Vertical Winds, *Planet Space Sci*, 32, 685, doi:10.1016/0032-
682 0633(84)90093-X, 1984.
- 683 Sakanoi, T., Fukunishi, H., Okano, S., Sato, N., Yamagishi, H., and Yukimatu, A. S.: Dynamical coupling of neutrals and ions
684 in the high-latitude *F* region: Simultaneous FPI and HF radar observations at Syowa Station, Antarctica, *Journal of*
685 *Geophysical Research: Space Physics*, 107, doi:10.1029/2001JA007530, 2002.
- 686 Shinagawa, H. and Oyama, S.: A two-dimensional simulation of thermospheric vertical winds in the vicinity of an auroral arc,
687 *Earth Planets Space*, 58, doi:10.1186/BF03352007, 2006.
- 688 Shiokawa, K., Katoh, Y., Satoh, M., Ejiri, M. K., and Ogawa, T.: Integrating-sphere calibration of all-sky cameras for
689 nightglow measurements, *Adv Space Res*, 26, 1025-1028, doi:10.1016/S0273-1177(00)00052-1, 2000.
- 690 Singh, R., Scipión, D. E., Kuyeng, K., Condor, P., Flores, R., Pacheco, E., de la Jara, C., and Manay, E.: Ionospheric Responses
691 to an Extreme (G5-Level) Geomagnetic Storm Using Multi-Instrument Measurements at the Jicamarca Radio
692 Observatory on 10-11 October 2024, *J Geophys Res-Space*, 130, ARTN e2024JA033642, doi:10.1029/2024JA033642,
693 2025.
- 694 Smith, R. W. and Hernandez, G.: Vertical Winds in the Thermosphere within the Polar-Cap, *J Atmos Terr Phys*, 57, 611-620,
695 doi:10.1016/0021-9169(94)00101-S, 1995.
- 696 Sobolev, V. V., Irvine, W. M., Gendel, M., and Lane, A. P.: Light scattering in planetary atmospheres, 1st . International series
697 of monographs in natural philosophy vol.76, Pergamon Press, Oxford, New York, doi:10.1016/C2013-0-05661-7, 1975.
- 698 Themens, D. R., Elvidge, S., McCaffrey, A., Jayachandran, P. T., Coster, A., Varney, R. H., Galkin, I., Goodwin, L. V., Watson,
699 C., Maguire, S., Kavanagh, A. J., Zhang, S. R., Goncharenko, L., Bhatt, A., Dorrian, G., Groves, K., Wood, A. G., and
700 Reid, B.: The High Latitude Ionospheric Response to the Major May 2024 Geomagnetic Storm: A Synoptic View,
701 *Geophysical Research Letters*, 51, e2024GL111677, doi:10.1029/2024GL111677, 2024.
- 702 Wang, C., Xu, J., Chen, Z., Li, H., Feng, X., Huang, Z., and Wang, J.: China's Ground-Based Space Environment Monitoring
703 Network—Chinese Meridian Project (CMP), *Space Weather*, 22, doi:10.1029/2024sw003972, 2024.
- 704 Wang, X., Aa, E., Chen, Y., Zhang, J., Zhu, Y., Cai, L., Lu, X., Luo, B., Liu, S., Li, M., Shen, H., and Yuan, T.: Midlatitude
705 Neutral Wind Response During the Mother's Day Super-Intense Geomagnetic Storm in 2024 Using Observations From
706 the Chinese Meridian Project, *Journal of Geophysical Research: Space Physics*, 130, e2024JA033574,
707 doi:10.1029/2024JA033574, 2025.
- 708 Wei, D., Zhu, Y., Liu, J., Gong, Q., Kaufmann, M., Olschewski, F., Knieling, P., Xu, J., Koppmann, R., and Riese, M.:
709 Thermally stable monolithic Doppler asymmetric spatial heterodyne interferometer: optical design and laboratory
710 performance, *Optics Express*, 28, doi:10.1364/oe.394101, 2020.



- 711 Wu, Q., Yuan, W., Xu, J. Y., Huang, C., Zhang, X. X., Wang, J. S., and Li, T.: First U.S.-China joint ground-based Fabry-
712 Perot interferometer observations of longitudinal variations in the thermospheric winds, *J Geophys Res-Space*, 119, 5755-
713 5763, doi:10.1002/2014ja020089, 2014.
- 714 Xu, H., Shiokawa, K., Oyama, S., and Otsuka, Y.: Thermospheric wind variations observed by a Fabry-Perot interferometer
715 at Tromsø, Norway, at substorm onsets, *Earth Planets Space*, 71, ARTN 93, doi:10.1186/s40623-019-1072-0, 2019.
- 716 Yang, C., Zhao, B., Jin, Y., Huang, C., Yao, X., and Wan, W.: Climatology of Nighttime Upper Thermospheric Winds From
717 Fabry-Perot Interferometer 2011–2019 Measurements Over Kelan (38.7°N, 111.6°E), China: Local Time, Seasonal, Solar
718 Cycle, and Geomagnetic Activity Dependence, *Journal of Geophysical Research: Space Physics*, 125, e2020JA027892,
719 doi:10.1029/2020JA027892, 2020.
- 720 Yu, T., Huang, C., Zhao, G. X., Mao, T., Wang, Y. G., Zeng, Z. C., Wang, J. S., and Xia, C. L.: A preliminary study of
721 thermosphere and mesosphere wind observed by Fabry-Perot over Kelan, China, *J Geophys Res-Space*, 119, 4981–4997,
722 doi:10.1002/2013ja019492, 2014.
- 723 Yuan, W., Xu, J. Y., Ma, R. P., Wu, Q. A., Jiang, G. Y., Gao, H., Liu, X. A., and Chen, S. Z.: First observation of mesospheric
724 and thermospheric winds by a Fabry-Perot interferometer in China, *Chinese Sci Bull*, 55, 4046–4051, doi:10.1007/s11434-
725 010-4192-2, 2010.
- 726 Zhang, K. D., Wang, H., Liu, J., Song, H. M., and Xia, H.: The Quasi-Periodic Nighttime Traveling Ionospheric Disturbances
727 on 13 May 2024 During the Recovery Phase of a SuperStorm, *J Geophys Res-Space*, 130, ARTN e2024JA033257,
728 doi:10.1029/2024JA033257, 2025.
- 729 Zhu, G., Zhu, Y., Kaufmann, M., Wang, T., Liu, W., and Xu, J.: An Efficient Calibration System of Optical Interferometer for
730 Measuring Middle and Upper Atmospheric Wind, *Remote Sensing*, 15, doi:10.3390/rs15071898, 2023.